23rd ABCM International Congress of Mechanical Engineering
December 6-11, 2015, Rio de Janeiro, RJ, Brazil

ON THE NONLINEAR EVOLUTION OF GÖRTLER VORTICES BY THE PRESENCE OF PRESSURE GRADIENT

J. K. Rogenski
Instituto de Ciências Matemáticas e de Computação, Universidade de São Paulo
josuelkr@gmail.com

J. M. Floryan
Western Engineering, The University of Western Ontario
mfloryan@eng.uwo.ca

L. F. de Souza
Instituto de Ciências Matemáticas e de Computação, Universidade de São Paulo
lefraso@icmc.usp.br

Abstract. *The laminar flow over a concave surface may undergo the turbulence state by secondary instabilities associated with the presence of longitudinal vortices known as Görtler vortices. Due to non-linearities these vortices distort the boundary layer structure by modifying the streamwise velocity component in both spanwise and normal to the wall directions. Nonlinear numerical simulation studies have been conducted to identify the role of external pressure gradient distributions in the development and saturation of the Görtler vortices. The results show the flow with adverse pressure reaches saturation upstream in comparison with neutral and favorable pressure distribution cases. Spanwise-mean shear stress values greater than the laminar baseflow ones are observed in the transition region.*

Keywords: *Görtler vortices, external pressure gradient, saturation, numerical simulation*

1. INTRODUCTION

The inviscid mechanism of the centrifugal instability may lead to the formation of counter-rotating vortices in situations where the pressure gradient in the radial direction is not strong enough to balance the centrifugal force. In boundary layer flows these vortices are known as Görtler vortices, and they develop in an open system with a weakly nonparallel basic state (Saric, 1994).

The nature of Görtler instability is weak. For this reason Görtler vortices themselves do not cause the laminar state to break down to turbulence directly. However these vortices distort the boundary layer basic state. Inflectional points in the streamwise velocity in both spanwise and normal to wall directions can be observed in this new configuration. The new and inflectional velocity profile is likely unstable to disturbances.

Experimental and numerical studies have been carried out to understand the transition process via the centrifugal instability. Comprehensive discussions regarding Görtler vortices are provided by Hall (1990), Floryan (1991) and Saric (1994). Some early investigations are focused on how flow configurations may affect the transition process. Local and nonlocal linear theories and the marching procedure are usually adopted to solve the system of equation. Studies of the curvature variation influence in the development of Görtler vortices are provided by Benmalek and Saric (1994). The authors support concave and zero-curvature geometry configurations are able to suppress Görtler vortices growth. The external pressure gradient influence is topic of discussion in Goulpié *et al.* (1996) and Marxen (2005).

This paper is focused on the investigation of the influence of an external pressure gradient different from the neutral case in a region where velocity profiles are inflectional and nonlinear effects are important. The problem is formulated based on the Navier-Stokes system of equations written in the vorticity-velocity formulation. Solutions are obtained by use of a parallel code based on a high-order, pseudo-spectral numerical simulation method. Results show that a favorable pressure gradient distribution has a stabilizing effect on the vortices. We also support the nonlinear nature of Görtler vortices leads to an increase of shear stress spanwise-mean values in comparison with a laminar baseflow state.

2. PROBLEM FORMULATION

Stability analyses are done considering a mean-flow state represented by a two-dimensional boundary layer flow over a slightly concave surface. Assuming a flow quantity $\widetilde{g}$ represented by

$$\widetilde{g} = g_b + g, \tag{1}$$

where g_b is the mean-flow state, the following dimensionless transport equations in the streamwise (x), wall-normal (y) and spanwise (z) directions can be used to represent the disturbances of the flow (Souza *et al.*, 2004; Malatesta *et al.*, 2013):

$$\frac{\partial \omega_x}{\partial t} + \frac{\partial a}{\partial y} - \frac{\partial b}{\partial z} + \frac{Go^2}{Re}\frac{\partial d}{\partial z} = \nabla^2 \omega_x, \tag{2}$$

$$\frac{\partial \omega_y}{\partial t} + \frac{\partial c}{\partial z} - \frac{\partial a}{\partial x} = \nabla^2 \omega_y, \tag{3}$$

$$\frac{\partial \omega_z}{\partial t} + \frac{\partial b}{\partial x} - \frac{\partial c}{\partial y} - \frac{Go^2}{Re}\frac{\partial d}{\partial x} = \nabla^2 \omega_z. \tag{4}$$

The ω_x, ω_y and ω_z are the components of the vorticity vector. We define vorticity as the opposite of the velocity vector $(u, v, w)^t$. Variable t is the time and $\nabla^2 = \left(\frac{1}{Re}\frac{\partial^2}{\partial x^2} + \frac{\partial^2}{\partial y^2} + \frac{1}{Re}\frac{\partial^2}{\partial z^2}\right)$. Re and Go are the Reynolds and Görtler numbers, respectively. Identifying dimensional quantities by an asterisk and assuming U^*_∞ is the potential streamwise velocity at an L^* position from the leading edge, nondimensionalization relations hold for

$$x = \frac{x^*}{L^*},\ \ y = \frac{1}{\sqrt{Re}}\frac{y^*}{L^*},\ \ z = \frac{z^*}{L^*},$$

$$u = \frac{u^*}{U^*_\infty},\ \ v = \frac{1}{\sqrt{Re}}\frac{v^*}{U^*_\infty},\ \ w = \frac{w^*}{U^*_\infty},$$

$$\omega_x = \frac{1}{Re}\frac{\omega_x^* L^*}{U^*_\infty},\ \ \omega_y = \frac{\omega_y^* L^*}{U^*_\infty},\ \ \omega_z = \frac{1}{Re}\frac{\omega_z^* L^*}{U^*_\infty}.$$

Functions a, b and c express nonlinear terms. The curvature influence is represented by d (Floryan and Saric, 1982). These functions are

$$a = \omega_x(v_b + v) - \omega_y(u_b + u), \tag{5}$$

$$b = \omega_{zb}u + \omega_z(u_b + u) - \omega_x w, \tag{6}$$

$$c = \omega_y w - \omega_{zb}v - \omega_z(v_b + v), \tag{7}$$

$$d = 2u_b u + u^2. \tag{8}$$

Velocity and vorticity components are correlated by

$$\frac{\partial^2 u}{\partial x^2} + \frac{\partial^2 u}{\partial z^2} = -\frac{\partial \omega_y}{\partial z} - \frac{\partial^2 v}{\partial x \partial y}, \tag{9}$$

$$\frac{1}{Re}\frac{\partial^2 v}{\partial x^2} + \frac{\partial^2 v}{\partial y^2} + \frac{1}{Re}\frac{\partial^2 v}{\partial z^2} = -\frac{\partial \omega_z}{\partial x} + \frac{\partial \omega_x}{\partial z}, \tag{10}$$

$$\frac{\partial^2 w}{\partial x^2} + \frac{\partial^2 w}{\partial z^2} = \frac{\partial \omega_y}{\partial x} - \frac{\partial^2 v}{\partial y \partial z}. \tag{11}$$

The continuity equation

$$\frac{\partial u}{\partial x} + \frac{\partial v}{\partial y} + \frac{\partial w}{\partial z} = 0, \tag{12}$$

and convenient boundary conditions close the system for disturbances (Souza *et al.*, 2004; Malatesta *et al.*, 2013).

The two-dimensional transport equation

$$\frac{\partial \omega_{zb}}{\partial t} + \frac{\partial u_b \omega_{zb}}{\partial x} + \frac{\partial v_b \omega_{zb}}{\partial y} = \frac{1}{Re}\frac{\partial^2 \omega_{zb}}{\partial x^2} + \frac{\partial^2 \omega_{zb}}{\partial y^2}, \tag{13}$$

the continuity equation

$$\frac{\partial u_b}{\partial x} + \frac{\partial v_b}{\partial y} = 0, \tag{14}$$

and the Poisson equation

$$\frac{1}{Re}\frac{\partial^2 v_b}{\partial x^2} + \frac{\partial^2 v_b}{\partial y^2} = -\frac{\partial \omega_{zb}}{\partial x} \tag{15}$$

are considered to represent the boundary layer mean flow.

Our baseflow solution should represent boundary layer flows with pressure gradient distribution different from the neutral case. In this sense we assume the potential flow is represented by

$$U_e = x^m, \tag{16}$$

where m is a local constant associated with the Hartree parameter (γ) by $\gamma = \frac{2m}{m+1}$.

The potential flow velocity and the pressure gradient may be related by the Bernoulli equation

$$U_e \frac{dU_e}{dx} + \frac{dp}{dx} = 0, \tag{17}$$

considering $U_e(x = 1) = 1$.

Baseflow boundary conditions are considered in accordance with Kloker *et al.* (1993).

3. NUMERICAL METHOD

The geometry of our numerical domain is sketched in Fig. 1. The inflow boundary is represented by $x = x_0$. Flow exits at $x = x_{max}$.

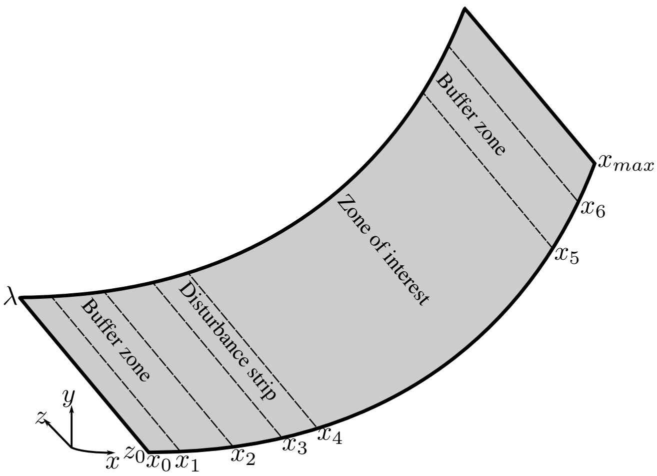

Figure 1. Sketch of our numerical domain. Buffer zones are inserted near inflow and outflow boundaries. A disturbance strip is also shown.

Buffer zones are artificially inserted between points x_1 and x_2 and between x_5 and x_6. These buffer zones are applied in accordance with Kloker *et al.* (1993). Disturbances are generated via blowing and suction of mass at the wall in the region between points x_3 and x_4.

Due to the spanwise quasi-periodic characteristic of the Görtler vortices (Ito, 1980) we can represent the flow quantity $g = \{u, v, w, \omega_x, \omega_y, \omega_z, a, b, c, d\}$ as a linear combination of $K + 1$ Fourier modes

$$g(x, y, z, t) = \sum_{k=0}^{K} g_k(x, y, t) e^{-\iota k \beta z}, \tag{18}$$

where ι is the imaginary unit. Here β represents the spanwise wavenumber

$$\beta = \frac{2\pi}{\lambda}, \tag{19}$$

and λ is the dimensionless wavelength of a pair of vortices.

Equations (2) - (12) are expressed for each Fourier mode k, as

$$\frac{\partial \omega_{xk}}{\partial t} + \frac{\partial a_k}{\partial y} + \iota k \beta b_k - \iota k \beta d_k = \nabla_k^2 \omega_{xk} \tag{20}$$

$$\frac{\partial \omega_{yk}}{\partial t} - \iota k \beta c_k - \frac{\partial a_k}{\partial x} = \nabla_k^2 \omega_{yk} \tag{21}$$

$$\frac{\partial \omega_{zk}}{\partial t} + \frac{\partial b_k}{\partial x} - \frac{\partial c_k}{\partial y} - \frac{\partial d_k}{\partial x} = \nabla_k^2 \omega_{zk} \tag{22}$$

$$\frac{\partial^2 u_k}{\partial x^2} - k^2 \beta^2 u_k = \iota k \beta \omega_{yk} - \frac{\partial^2 v_k}{\partial x \partial y} \tag{23}$$

$$\nabla_k^2 v_k = -\frac{\partial \omega_{zk}}{\partial x} - \iota\beta\omega_{xk} \tag{24}$$

$$\frac{\partial^2 w_k}{\partial x^2} - k^2\beta^2 w_k = \frac{\partial \omega_{yk}}{\partial x} + \iota k\beta\frac{\partial v_k}{\partial y}, \tag{25}$$

$$\frac{\partial u_k}{\partial x} + \frac{\partial v_k}{\partial y} - \iota k\beta w_k = 0, \tag{26}$$

where $\nabla_k^2 = \left(\frac{1}{Re}\frac{\partial^2}{\partial x^2} + \frac{\partial^2}{\partial y^2} - \frac{1}{Re}k^2\beta^2\right)$.

All disturbance calculations are done in the Fourier space but nonlinear products. The streamwise and normal to the wall derivatives are approximated by compact finite difference schemes (Souza *et al.*, 2005). Spanwise derivatives are calculated straightforward. For a k Fourier mode, Eqs. (20)-(22) are solved by the use of a 4^{th} order Runge-Kutta method. At each substep of the temporal integrator: (a) the system of linear equations obtained through the discretization of Eq. (24) is solved by a geometric multigrid method (Rogenski *et al.*, 2015). (b) streamwise and spanwise components of the disturbance velocity are calculated by solving the $1D$ Poisson equations (Eqs. (23) and (25)). (c) vorticity components are updated in the wall. In the last substep of the Runge-Kutta method, vorticity components are filtered by the use of a compact tridiagonal filter (Lele, 1992). A stationary state is assumed to be reached when the maximum difference between the $k = 1$ spanwise vorticity component is smaller than a given small parameter.

The mean flow state is assumed to be a quasi-$2D$ solution of the Navier-Stokes system of equations. Flow variables are calculated in the physical space. Calculations follow a simplified version of the described disturbance algorithm.

3.1 The boundary conditions

Due to the use of buffer zones close to inflow and outflow boundaries, disturbance values of vorticity and velocity may be consider to be equal to zero. Periodicity is assumed in the spanwise direction. The no-slip and impermeability conditions are assumed for the velocity vector at the rigid boundary but disturbance strip.

At the disturbance generator the v_1 velocity component is imposed to have a $\sin^3$ shape. Vorticity components at the wall are calculated by the use of the expressions

$$\frac{\partial^2 \omega_{x_k}}{\partial x^2} - k^2\beta^2\omega_{x_k} = -\frac{\partial^2 \omega_{y_k}}{\partial x \partial y} - \beta\nabla_k^2 v_k, \tag{27}$$

$$\omega_{y_k} = 0, \tag{28}$$

$$\frac{\partial \omega_{z_k}}{\partial x} = \iota k\beta\omega_{x_k} - \nabla_k^2 v_k. \tag{29}$$

Our numerical domain is chosen to be high enough to ensure vorticity components are equal zero. At the upper boundary the continuity equation is assured and $\frac{\partial v_k}{\partial y} = 0$.

The no-slip and impermeability conditions are also assumed for the baseflow calculations. The vorticity component is calculated considering the two-dimensional

$$\frac{\partial \omega_{z_b}}{\partial x} = -\nabla^2 v_b. \tag{30}$$

At the inflow boundary velocity and vorticity components of the baseflow are assumed to be equal to a Falkner-Skan similar solution. At the upper boundary the meanflow is assumed to be non-rotational. The u_b velocity component is assumed to be represented by a power of the the streamwise position x (see Eq. 16). At the outflow, second derivate of the quantities in the streamwise direction are considered to be zero.

4. RESULTS

Nonlinear simulations are carried out considering the same physical parameters of the classical experiments of Swearingen and Blackwelder (1987). We consider the radius of the concave surface $R^* = 3.2\ m$. For all simulations the external velocity is $U_\infty^* = 5.0\ m.s^{-1}$ in $L^* = 0.1\ m$. Kinematic viscosity is $\nu^* = 1.5 \times 10^{-5}\ m^2.s^{-1}$.

The Reynolds and Görtler numbers are defined in a streamwise position L^*. We assume

$$Re = \frac{U_\infty^* L^*}{\nu^*} \text{ and } Go = Re^{\frac{1}{4}}\sqrt{\frac{L^*}{R^*}}. \tag{31}$$

The spanwise wavelength of the vortices is defined in terms of the characteristic wavelength parameter

$$\Lambda = \frac{U_\infty^* \lambda^*}{\nu^*}\sqrt{\frac{\lambda^*}{R^*}}. \tag{32}$$

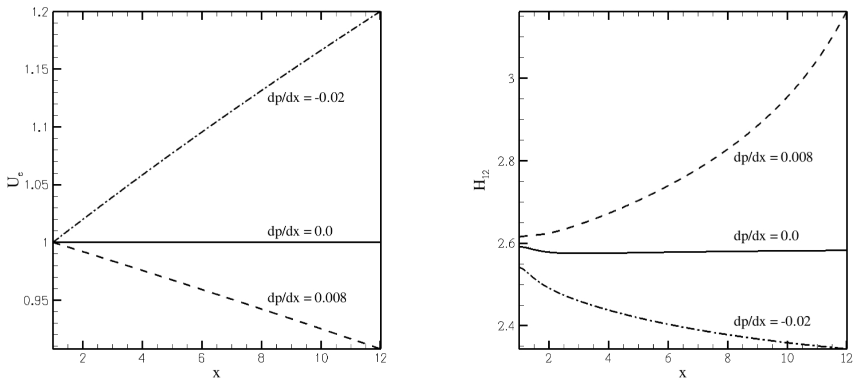

(a) external streamwise velocity U_e (b) shape factor H_{12}

Figure 2. Baseflow characteristics for three different external pressure distributions.

The $\Lambda = 160$ and 450 characteristic values are considered as test cases. For each case, three different external pressure gradient configurations are investigated: a favorable case $dp/dx = -0.02$, an adverse case $dp/dx = 0.008$ and the neutral case $dp/dx = 0.0$. The external streamwise velocity U_e and shape factor H_{12} for the three cases are presented by Fig. 2.

Simulations adopt 11 Fourier modes with 32 points in the physical space. For each Fourier mode a $2D$ y-stretched mesh is adopted. We consider 2201 points in the x-direction with step size $dx = 5.0 \times 10^{-3}$. In the y-direction 225 points with first step size $dy = 8.0 \times 10^{-2}$ and stretching factor $sf = 1\%$ are used. The time step is 2.5×10^{-3}. Buffer zones and the disturbance region are defined close to the boundaries as $[x_0;\ x_1;\ \ldots;\ x_{max}] = [1;\ 1;\ 1.28;\ 1.48;\ 1.88;\ 11;\ 11.75;\ 12]$. A stationary state is reached assuming the maximum difference between ω_{z1} values smaller than 5×10^{-10} in a numerical iteration. Different sets of numerical parameters have been tests and the following results are considered to be grid-independent. The numerical code and model have been verified and validated through Linear Stability Theory, numerical, and experimental literature results.

The energy of a Fourier mode

$$E_k(x) = \int_0^\infty |u_k|^2 \, dy \tag{33}$$

is adopted as a metric for disturbance evolution.

In Fig. 3, the energy for all Fourier modes $k = 0, \ldots, K$ is presented for the development of $\Lambda = 160$ vortices in the favorable pressure gradient regime $(dp/dx = -0.02)$. The interaction between different modes is similar to the energy behavior presented in neutral cases (Li and Malik, 1995). The fundamental mode $(k = 1)$ shows the highest energy level in the linear region. Linear growth of all modes can be observed for $x < 6$. Further downstream nonlinear effects become more significant and saturation occurs.

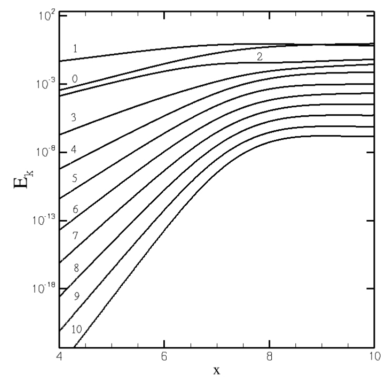

Figure 3. The disturbance evolution of $\Lambda = 160$ vortices in a favorable pressure gradient regime $(dp/dx = -0.02)$. The energy of all Fourier modes $k = 0, \ldots, K - 1$ are presented.

The fundamental and baseflow correction $(k = 0)$ modes for the adverse, neutral and favorable tests of $\Lambda = 160$ vortices are shown in Fig. 4(a). In Fig. 4(b), $\Lambda = 450$ vortices are also considered.

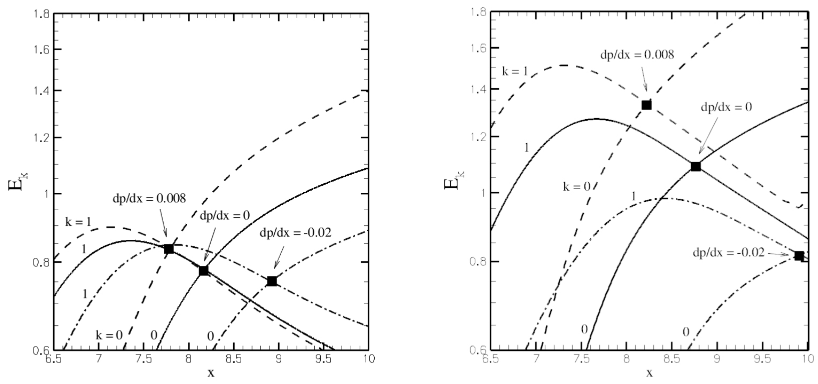

(a) $\Lambda = 160$ (b) $\Lambda = 450$

Figure 4. Baseflow correction and fundamental modes for the adverse, neutral and favorable pressure gradient cases.

Aimed to compare the influence of the external pressure gradient in the saturation of the Görtler vortices, we consider the intercept point of the fundamental and baseflow correction modes as a "measure of saturation". In the Fig. 4(a-b), the square symbols label saturation region for each pressure distribution case. In addiction Tab. 1 quantifies the streamwise position of these square symbols for all cases.

Table 1. Streamwise position of the intercept point between the fundamental and baseflow corrections modes.

	$dp/dx = 0.008$	$dp/dx = 0.0$	$dp/dx = -0.02$
$\Lambda = 160$	7.77	8.16	8.93
$\Lambda = 450$	8.22	8.77	9.91

It can be observed that for both wavenumber parameters ($\Lambda = 160$ and 450) the adverse pressure case saturates first. It is followed by the neutral and favorable pressure gradient cases.

Near the saturation region, the streamwise velocity profile in a $z \times y$ plane presents the well known mushroom structure for a neutral baseflow distribution (Schrader *et al.*, 2011; Sescu and Thompson, 2015). In Fig. 5 the streamwise velocity isocontours of $\Lambda = 160$ and $\Lambda = 450$ vortices are presented for the three external pressure distribution. Left, middle and right columns represent the favorable($dp/dx = -0.02$), neutral($dp/dx = 0.0$) and adverse($dp/dx = 0.008$) cases, respectively. The streamwise velocity of each case is illustrated considering $x = 9$. Isolines start with $\widetilde{u} = 0.1$ close to the wall with increments of 0.1. The typical mushroom vortical structures can be observed for all the three pressure distributions. A comparison between different pressure gradient cases demonstrates the size of the vortices in the adverse pressure regime is bigger than the neutral and favorable cases. For the same pressure gradient configurations $\Lambda = 450$ vortices seems to be more energetic than $\Lambda = 160$ ones.

By Fig. 5 one may noticed that due to nonlinear effects the classical downwash region generated by the Görtler vortices seems to be larger than the upwash one for the presented favorable pressure gradient case. The observed difference between the downwash and upwash regions may modify wall shear stress quantities. In Fig. 6 the spanwise-mean shear stress τ is presented as a function of the streamwise positions for all cases. The shear stress values for baseflow configurations are presented for comparison. Based on Fig. 6 it is clear the presence of nonlinearities associated with the Görtler vortices alter the spanwise-mean wall shear stress values. The streamwise position $x = 3$ may be chosen to represent the position in which spanwise-mean wall shear stress starts to increase in comparison with baseflow values. For all cases, the spanwise-mean wall shear stress increases downstream. Close to saturation region the metric seems to reach a plateau region and to start to decay slowly.

By keeping the external pressure gradient fixed the $\Lambda = 160$ case presents higher shear stress values than the $\Lambda = 450$ case. This fact leads us to generalization the smaller the size of vortices the greater the spanwise-mean wall shear stress. It is also important to noticed that favorable external pressure distributions present the highest values of the metric.

In Tab. 2 the percentage increase in relation to the baseflow cases is shown for three different streamwise positions in the region where nonlinear effects are important. An increase up to approximately five times the baseflow value (490%) can be observed for $\Lambda = 160$ vortices in the adverse pressure case $dp/dx = 0.008$. The less significant variation provided by Tab. 2 refers to the increase of 38% considering the evolution of $\Lambda = 450$ vortices in the favorable regime $(dp/dx = -0.02)$. As expected, by fixing the streamwise position and the pressure gradient case, the $\Lambda = 160$ vortices always present the highest variation.

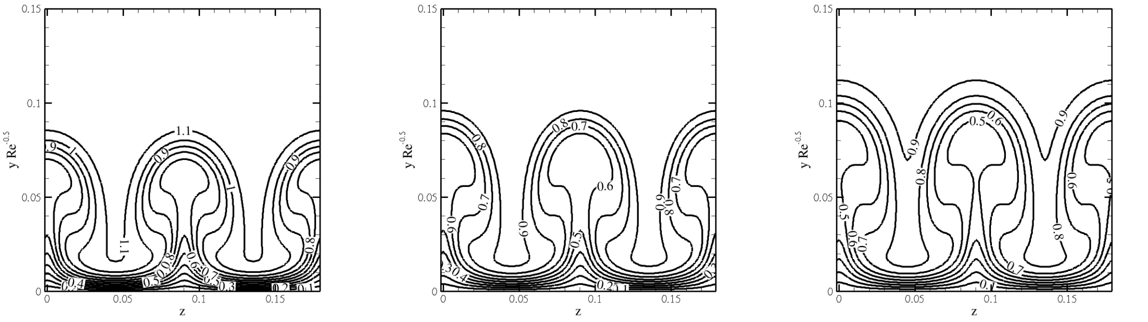

(a) $dp/dx = -0.02$ and $\Lambda = 160$ (b) $dp/dx = 0.0$ and $\Lambda = 160$ (c) $dp/dx = 0.008$ and $\Lambda = 160$

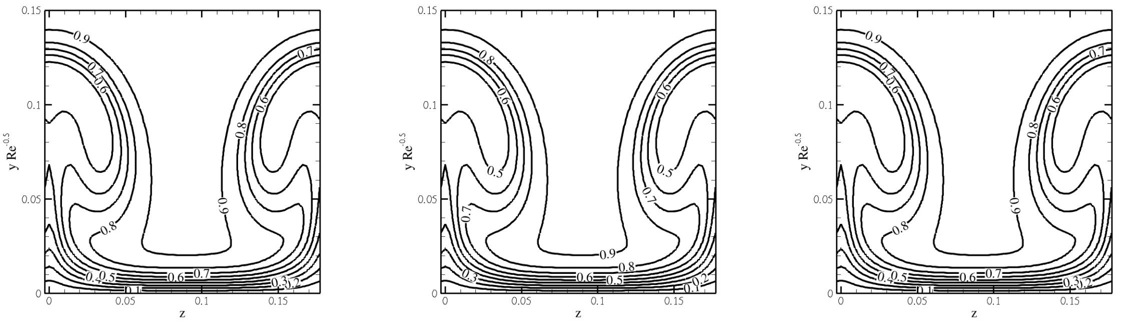

(d) $dp/dx = -0.02$ and $\Lambda = 450$ (e) $dp/dx = 0.0$ and $\Lambda = 450$ (f) $dp/dx = 0.008$ and $\Lambda = 450$

Figure 5. $\widetilde{u}$ velocity component isocontour in a $z \times y$ plane of $\Lambda = 160$ and $\Lambda = 450$ Görtler vortices. The streamwise positions $x = 9$ is illustrated. Lines represent velocity values starting from 0.1 and increments of 0.1. Left, center and right columns represent favorable $(dp/dx = -0.02)$, neutral$(dp/dx = 0.0)$ and adverse$(dp/dx = 0.008)$ cases, respectively.

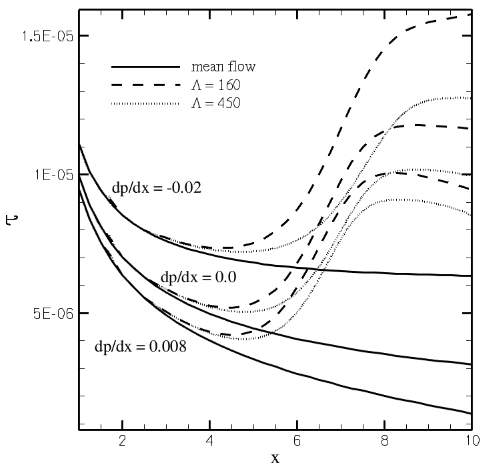

Figure 6. Spanwise-mean wall shear stress (τ) as a function of the streamwise position for all cases under consideration. Straight lines represent meanflow boundary layer profiles. Dashed and dotted lines denote $\Lambda = 160$ and $\Lambda = 450$ vortices, respectively.

5. CONCLUSIONS

The nonlinear development of the centrifugal instability in adverse, neutral and favorable boundary layer regimes has been investigated by the use of a high-order numerical simulation code. Results show disturbances in an adverse pressure gradient boundary layer configuration may reach saturation upstream in comparison with neutral and favorable cases. We also observe that the non-linear evolution of the Görtler vortices leads to an increase in the spanwise-mean shear stress values in comparison with the laminar baseflow state. The size of the Görtler vortices and the thickness of the boundary

Table 2. Percentage increase of the spanwise-mean wall shear stress in relation to the baseflow pressure gradient cases for three different streamwise positions.

		$dp/dx = 0.008$	$dp/dx = 0.0$	$dp/dx = -0.02$
$x = 7$	$\Lambda = 160$	270	172	79
	$\Lambda = 450$	222	122	38
$x = 8$	$\Lambda = 160$	399	229	126
	$\Lambda = 450$	350	183	77
$x = 9$	$\Lambda = 160$	490	255	143
	$\Lambda = 450$	436	206	98

layer have relevant influence on the shear stress behavior.

6. ACKNOWLEDGEMENTS

The São Paulo Research Foundation (FAPESP) is acknowledged for financial support under grants #2011/08010-0 and #2013/00553-0. The authors thank SHARCNET consortium for computational time. Josuel thanks Prof. M. T. de Mendonça for gainful discussions.

7. REFERENCES

Benmalek, A. and Saric, W.S., 1994. "Effects of curvature variation on the nonlinear evolution of Goertler vortices". *Physics of Fluids*, Vol. 6, pp. 3353–3367.

Floryan, J.M., 1991. "On the Görtler instability of boundary layers". *Prog. Aerospace Sci.*, Vol. 28, pp. 235–271.

Floryan, J.M. and Saric, W.S., 1982. "Stability of Görtler vortices in boundary layers". *AIAA Journal*, Vol. 20, No. 3, pp. 316–324.

Goulpié, P., Klingmann, B.G.B. and Bottaro, A., 1996. "Görtler vortices in boundary layers with streamwise pressure gradient". *Physics of Fluids*, Vol. 8, pp. 451–459.

Hall, P., 1990. "Görtler vortices in growing boundary layer: the leading edge receptivity problem, linear growth and the nonlinear breakdown stage". *Mathematika*, Vol. 37, No. 74, pp. 151–189.

Ito, A., 1980. "The generation and breakdown of longitudinal vortices along a concave wall". *J. Japan Soc. Aero. Space Sci.*, Vol. 28, pp. 327–333.

Kloker, M., Konzelmann, U. and Fasel, H.F., 1993. "Outflow boundary conditions for spatial Navier-Stokes simulations in transition boundary layers". *AIAA Journal*, Vol. 31, No. 4, pp. 620–628.

Lele, S., 1992. "Compact finite difference schemes with spectral-like resolution". *Journal of Computational Physics*, Vol. 103, pp. 16–42.

Li, F. and Malik, M.R., 1995. "Fundamental and subharmonic secondary instability of Görtler vortices". *J. Fluid Mech.*, Vol. 297, pp. 77–100.

Malatesta, V., Souza, L.F. and Liu, J.T.C., 2013. "Influence of Goertler vortices spanwise wavelenght on heat transfer rates". *Computation Thermal Sciences: An International Journal*, Vol. 5, No. 5, pp. 389–400.

Marxen, O., 2005. *Numerical studies of physical effects related to the controlled transition process in laminar separation bubbles*. Ph.D. thesis, Universität Stuttgart.

Rogenski, J.K., Petri, L.A. and Souza, L.F., 2015. "Effects of parallel strategies in the transitional flow investigation". *J. Braz. Soc. Mech. Sci. Eng.*, Vol. 37, pp. 861–872.

Saric, W.S., 1994. "Görtler vortices". *Annual Review of Fluid Mechanics*, Vol. 26, pp. 379–409.

Schrader, L., Brandt, L. and Zaki, T.A., 2011. "Receptivity, instability and breakdown of Görtler flow". *J. Fluid Mech.*, Vol. 682, pp. 362–396.

Sescu, A. and Thompson, D., 2015. "On the excitation of Görtler vortices by distributed roughness elements". *Theoretical and Computational Fluid Dynamics*, Vol. 29, pp. 67–92.

Souza, L.F., Mendonça, M.T., de Medeiros, M.A.F. and Kloker, M., 2004. "Seeding of Görtler vortices through a suction and blowing strip". *Journal of the Brazilian Society of Mechanical Sciences*, Vol. XXVI, pp. 269–279.

Souza, L.F., Mendonça, M.T. and Medeiros, M.A.F., 2005. "The advantages of using high-order finite differences schemes in laminar-turbulent transition studies". *International Journal for Numerical Methods in Fluids*, Vol. 48, pp. 565–592.

Swearingen, J.D. and Blackwelder, R.F., 1987. "The growth and breakdown of streamwise vortices in the presence of a wall". *Journal of Fluid Mechanics*, Vol. 182, pp. 255–290.

8. RESPONSIBILITY NOTICE

The authors are the only responsible for the printed material included in this paper.